



**HAL**  
open science

## 2T3C HCA, a new hollow cylinder device using Digital Image Correlation to measure properties of interfaces between asphalt layers

T. Attia, H. Di Benedetto, C. Sauzéat, S. Pouget

### ► To cite this version:

T. Attia, H. Di Benedetto, C. Sauzéat, S. Pouget. 2T3C HCA, a new hollow cylinder device using Digital Image Correlation to measure properties of interfaces between asphalt layers. *Construction and Building Materials*, 2020, 247, pp.118499. 10.1016/j.conbuildmat.2020.118499 . hal-02966831

**HAL Id: hal-02966831**

**<https://hal.science/hal-02966831>**

Submitted on 22 Aug 2022

**HAL** is a multi-disciplinary open access archive for the deposit and dissemination of scientific research documents, whether they are published or not. The documents may come from teaching and research institutions in France or abroad, or from public or private research centers.

L'archive ouverte pluridisciplinaire **HAL**, est destinée au dépôt et à la diffusion de documents scientifiques de niveau recherche, publiés ou non, émanant des établissements d'enseignement et de recherche français ou étrangers, des laboratoires publics ou privés.



Distributed under a Creative Commons Attribution - NonCommercial 4.0 International License



36 correctly applied, the asphalt concrete layers are considered perfectly bonded in some  
37 of the current pavement design methods [3,4]. However, premature degradations linked  
38 with the debonding of the layers have been reported [5,6]. In this case, the pavement is  
39 subjected to loads it is not designed to resist to, implying a shortened lifetime. It is also  
40 possible that even for tack coat applied carefully and with a good dosage the interface  
41 will fail in fatigue before the asphalt concretes [7]. Yet, interface fatigue behavior is  
42 not considered in the design methods. The study of the mechanical behavior of inter-  
43 faces between asphalt concrete layers is then critical to help designing better roads.

44 The mechanical testing of interfaces began in the 1970's [1,8] and has gained more  
45 and more importance with time. Traffic and climate loads create complex stress states  
46 in the pavement. Different types of tests were developed to evaluate the bond strength  
47 at the interface between two asphalt pavement layers: tensile tests [9], shear tests [8,10-  
48 12], wedge splitting tests [9,13], torque test [14] (for broader overviews, see [15,16]).  
49 The shear tests are the most common and some of them can also apply compressive or  
50 tensile stress. Most of these tests aimed at evaluating only the shear strength of inter-  
51 faces, which is the highest possible shear stress the interface can endure before failing.  
52 The influence of factors such as temperature [17], normal stress application [10], nature  
53 and dosage of tack coat [18] have been investigated. Several shear tests are used to  
54 assess interface fatigue properties under cyclic shear loadings [2, 19-22] in order to  
55 obtain the fatigue law of interfaces for different test conditions or different materials.  
56 All these shear tests are inhomogeneous: the shear stress is not uniform at the interface.

57 It appears that a powerful test on interfaces should, (i) be able to apply shear and  
58 compressive/tensile stress, in monotonic or cyclic modes, to reproduce the actual pave-  
59 ment conditions, and (ii) be homogeneous in order to be analyzed correctly.

60 This paper presents the development of a new device to test interfaces between pave-  
61 ment layers. It is called 2T3C Hollow Cylinder Apparatus (2T3C HCA) and can apply  
62 torsion and tension-compression to hollow cylinder samples composed of two asphalt  
63 concrete layers. This apparatus uses 3D Digital Image Correlation (3D DIC) to observe  
64 the behavior of the interface. Additionally, the first experimental characterization of the  
65 viscoelastic behavior of asphalt concretes and of the interface using 2T3C HCA is pre-  
66 sented.

67 This work is part of the industrial chair Eiffage/ENTPE dedicated to pavement ma-  
68 terials and structures.

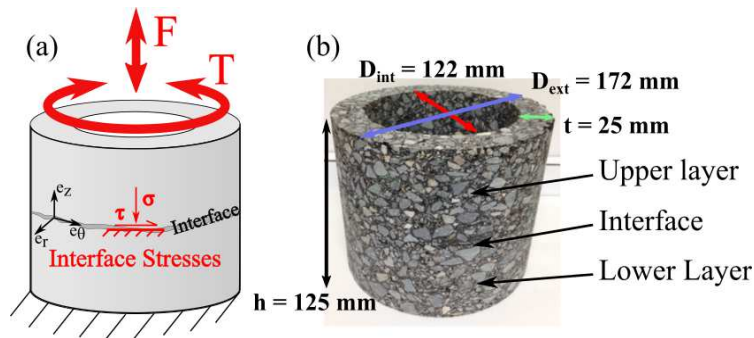
## 69 **2 Description of 2T3C Hollow Cylinder Apparatus (2T3C** 70 **HCA)**

### 71 **2.1 Hollow cylinder sample**

72 Applying a torque to a cylinder creates an inhomogeneous shear stress field. For  
73 example, if the material is elastic linear isotropic, the shear stress varies linearly with  
74 the radius, being nil at the center of the cylinder. In a hollow cylinder, the inner part of  
75 the cylinder is removed. If the thickness left is thin enough then one can consider that  
76 the shear stress is homogeneous with a good approximation [23] which ensures simpli-  
77 fied but accurate test analysis. This is why a hollow cylinder apparatus is relevant to  
78 study interfaces behavior. Hollow cylinder tests have been broadly used for the testing

79 of soils and granular materials [24,25] and they have also been used for the study of  
 80 asphalt concrete [26-28]. However, no example of application to the study of interfaces  
 81 between asphalt layers was found in the literature.

82 A new hollow cylinder apparatus has been developed at the University of  
 83 Lyon/ENTPE: it is called 2T3C (in French, *Torsion-Traction-Compression sur Cylin-*  
 84 *dre Creux*) Hollow Cylinder Apparatus (2T3C HCA). It allows applying torsion and  
 85 tension-compression to hollow cylinder samples. The sample dimensions are: height of  
 86 125 mm, internal diameter of 122 mm, external diameter of 172 mm and thickness of  
 87 25 mm. The sample section area is 115.5 cm<sup>2</sup>. The samples are composed of two asphalt  
 88 concrete layers with a tack coat at the interface located in the middle of the sample  
 89 (Figure 1). The external diameter and the height are chosen considering fabrication  
 90 constraints. The selected thickness is a compromise between having a thickness large  
 91 enough compared to the maximum aggregate size and small enough to obtain the max-  
 92 imum shear stress applicable and a good shear stress homogeneity. The ratio between  
 93 internal radius and external radius is 0.71, this value is between 0.65 and 0.82, the range  
 94 recommended for a reasonable assumption of homogeneity of shear stress for a hollow  
 95 cylinder test [23].



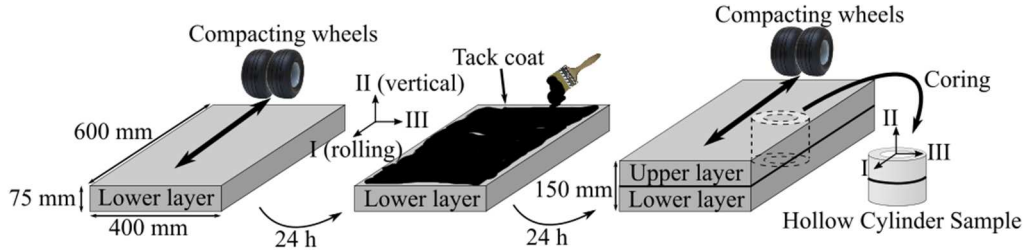
96

97

Fig. 1. 2T3C HCA hollow cylinder samples: (a) schematic, (b) picture

## 98 2.2 Sample preparation

99 In this section, the fabrication of laboratory samples is presented (Figure 2) but sam-  
 100 ples from real pavements cored *in situ* can also be tested with the 2T3C HCA. A slab  
 101 with two layers and a tack coat at the interface is created using the French wheel com-  
 102 pactor [29] (Figure 3). This is done in three steps. First, half a slab (600x400x75 mm<sup>3</sup>)  
 103 of the material representing the base course, the lower layer, is compacted. Then, after  
 104 a 24 h rest period, a tack coat made of asphalt emulsion is applied on the surface of the  
 105 lower layer using a brush (Figure 3). Finally, after another 24 h rest, the upper layer is  
 106 compacted using the compacting wheels again to get the complete slab (600x400x150  
 107 mm<sup>3</sup>).

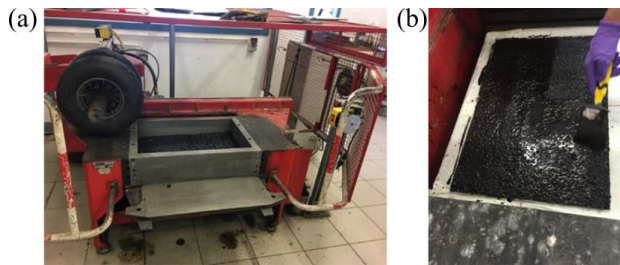


108

109

110

**Fig. 2.** Process to obtain hollow cylinder sample from a two layered slab with a tack coat at the interface



111

112

113

**Fig. 3.** French wheel compactor [29] (a) and tack coat application with brush (b) for the sample preparation

114

115

116

117

118

119

First the inside of a hollow cylinder is cored and then the outside. The two ends of the sample are then sawed to guarantee their planarity. A speckle pattern consisting of sprayed black paint over a thin white paint coat is applied on the surface of the sample for Digital Image Correlation (DIC) analysis. Samples are glued to aluminum plates using epoxy resin. A specially designed gluing device ensures that the axis of the hollow cylinder is coincident with the axes of the plates and thus of the hydraulic press.

120

### 2.3 2T3C HCA measuring systems

121

122

123

124

125

126

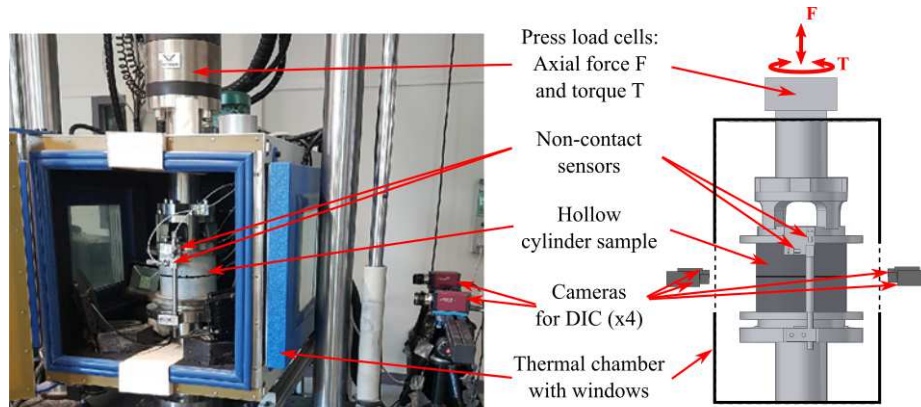
127

128

129

130

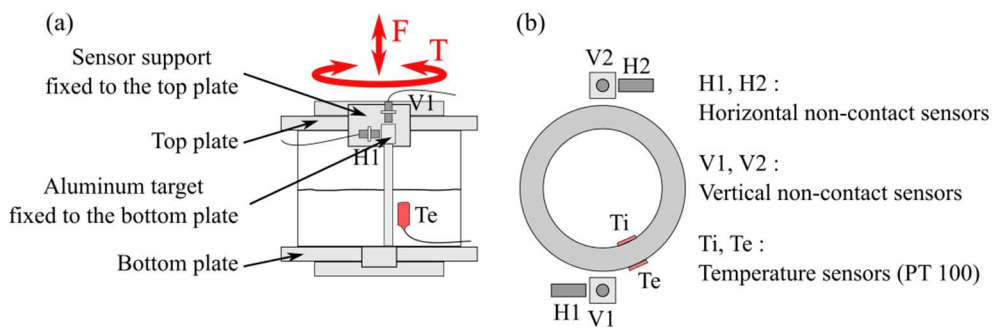
Torsion and tension-compression are applied to the samples using a servohydraulic press. Load cells measure the axial force up to  $\pm 100$  kN (with an accuracy of 0.010 kN) and the torque up to  $\pm 2$  kNm (accuracy of 0.1 Nm). Axial loadings and rotation loadings can be applied independently with any type of loading history: monotonic or cyclic (up to 10 Hz), stress or displacement controlled, following any load path. The sample with the plates, fixed to the press, is located in a thermal chamber with a temperature range from  $-20$  °C to  $+60$  °C (Figure 4). The temperature is measured on the surface of the sample with two PT100 sensors, one on the inside surface of the sample and one on the outside surface of the sample (Figure 5) in order to verify the homogeneity of the temperature field in the sample.



131  
132

**Fig. 4.** Picture and scheme of the 2T3C HCA with measuring systems

133 Two pairs of non-contact sensors measure the global displacements (in rotation and  
134 axial direction) between the top and the bottom of the samples. They can measure  
135 displacements with an accuracy of about  $0.1 \mu\text{m}$  on a  $1000 \mu\text{m}$  range. Sensors are fixed to  
136 the top plate and their aluminum target is fixed to the bottom plate. On each side of the  
137 sample there is one pair of non-contact sensors with one sensor that measures vertical  
138 displacement and one sensor that measures the displacement related to the rotation (Fig-  
139 ure 5). The value of global vertical displacement is taken as the average of the values  
140 of the two sensors measuring the vertical displacement (V1 and V2 in Figure 5). The  
141 global horizontal displacement related to the rotation is obtained in a similar way. Tests  
142 can be performed under displacement control using the non-contact sensors values.



143  
144

**Fig. 5.** 2T3C HCA sample instrumentation: (a) Side view, (b) Top view

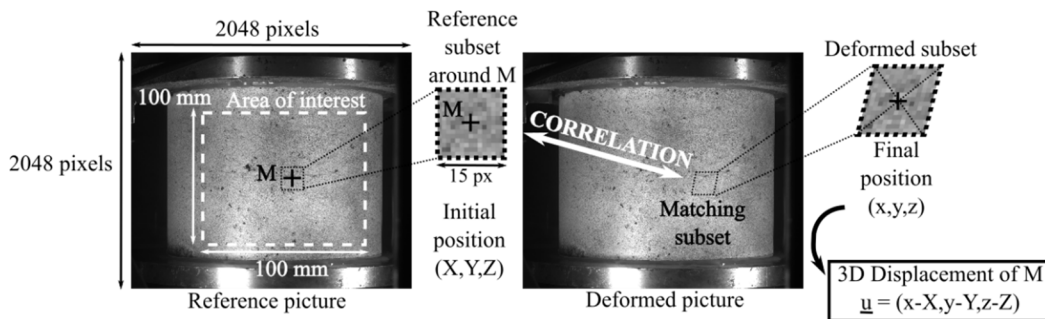
145 In addition to global measurements, a local optical measurement method, the 3D  
146 DIC is used in the 2T3C HCA. This method finds the displacement field in the three  
147 dimensions on the surface of the sample and is presented in the next section.

## 148 2.4 Analysis from Digital Image Correlation

149 Two pairs of CCD cameras take digital pictures of 4 Mpx of each side of the sample  
 150 (Figure 4) with a maximum acquisition frequency of 10 Hz. In each pair, the optical  
 151 axii of the two cameras form an angle of  $30^\circ$  in order to use 3D DIC. Cameras are  
 152 located outside the thermal chamber, 600 mm from the surface of the sample. At this  
 153 distance and considering the CCD sensor characteristics, one pixel of a picture repre-  
 154 sents  $150\ \mu\text{m}$  of material. The thermal chamber has windows on its sides, which makes  
 155 it possible to take pictures of the sample during tests at controlled temperature.

156 DIC principle is schematized in Figure 6. During a test, grayscale pictures of the  
 157 sample are taken at different levels of deformation. The first image, representing the  
 158 reference state, is called the reference picture. The goal of DIC is to obtain the displace-  
 159 ment of the points at the surface of the sample at each level of deformation, *i.e.* for each  
 160 picture, relatively to the reference state. For each pixel of the reference picture located  
 161 in the area of interest (area where displacements are researched), a subset of the picture  
 162 is selected. It is a square, usually a dozen pixels long, centered around the pixel. A  
 163 correlation algorithm finds the subset of the deformed picture that looks the most like  
 164 the subset in the reference picture and deduces the displacement of the pixel [30].

165 There needs to be a very contrasted and random pattern at the surface of the studied  
 166 material. Asphalt concretes samples are naturally not well-contrasted. A speckle pat-  
 167 tern, as the one described in section 2.2, is usually applied on the samples surface [31].  
 168 DIC has been used for the study of asphalt concretes cracking behavior [32] and rarely  
 169 for the study of interfaces [33]. It has proved to be a consistent tool in the study of  
 170 deformations of many materials such as cement concrete [34,35], glass [36] or metals  
 171 [37].



172

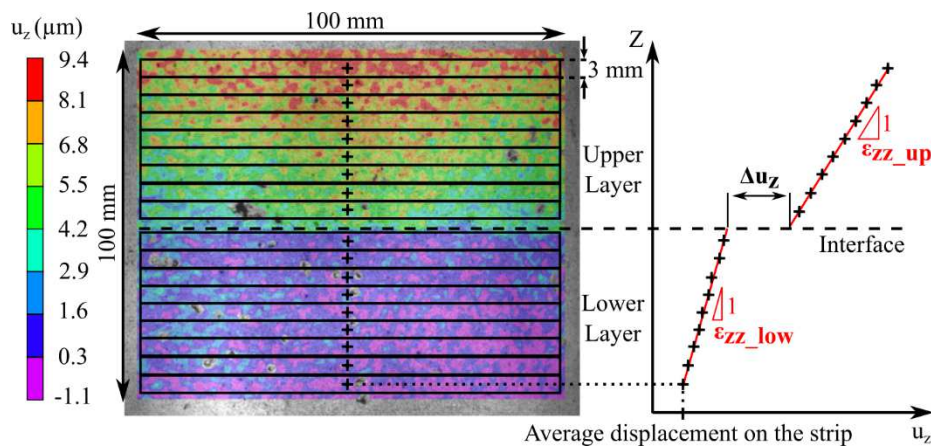
173 **Fig. 6.** 3D Digital Image Correlation: determination of 3D displacements of each point M of the  
 174 area of interest

175 For 3D DIC, two pictures of the same surface taken from different angles are needed  
 176 at each state of deformation. An algorithm between the two pictures associates a spatial  
 177 position to any pixel of the images. Displacements in the three dimensions are found  
 178 using the correlation algorithm between reference and deformed states on one image of  
 179 each pair [38].

180 The Vic-3D<sup>®</sup> software developed by Correlated Solutions is used for 3D DIC meas-  
 181 urements in the 2T3C HCA. It computes displacements in the three dimensions on the  
 182 hollow cylinder surface and expresses them in the cylindrical coordinate system related

183 to the hollow cylinder ( $u_r, u_\theta, u_z, Z$  being the axis of the cylinder). The heterogeneity of  
 184 the asphalt concretes induces high spatial variability of displacements due to the differ-  
 185 ence in mechanical behaviors of bitumen and aggregates. A specific analysis developed  
 186 at the ENTPE computes the three strain tensor components ( $\varepsilon_{\theta\theta}, \varepsilon_{zz}, \varepsilon_{\theta z}$ ) of both asphalt  
 187 concrete layers and the displacement gaps at the interface ( $\Delta u_z, \Delta u_\theta$ ) throughout a test,  
 188 anytime a picture is taken. Strain is obtained with an accuracy of about  $1 \mu\text{m}/\text{m}$  and  
 189 displacement gaps with an accuracy of  $0.1 \mu\text{m}$ .

190 For  $\varepsilon_{zz}$  computation, horizontal strips (100 mm long and 3 mm thick) are drawn on  
 191 the pictures as illustrated in Figure 7. The number of strips in each layer depends on the  
 192 sample dimensions (between 10 and 15). For each state of deformation, the displace-  
 193 ment component  $u_z$  is averaged on each strip and the average value is affected to the  
 194 coordinate  $Z$  of the center of the strip. The slopes of the lines obtained with linear re-  
 195 gressions in the diagram  $Z-u_z$ , one in each layer, give the strain components  $\varepsilon_{zz}$  in both  
 196 asphalt concretes. These two lines do not intersect at the interface and the gap between  
 197 them at the level of the interface (located visually) defines the axial displacement gap  
 198  $\Delta u_z$ .

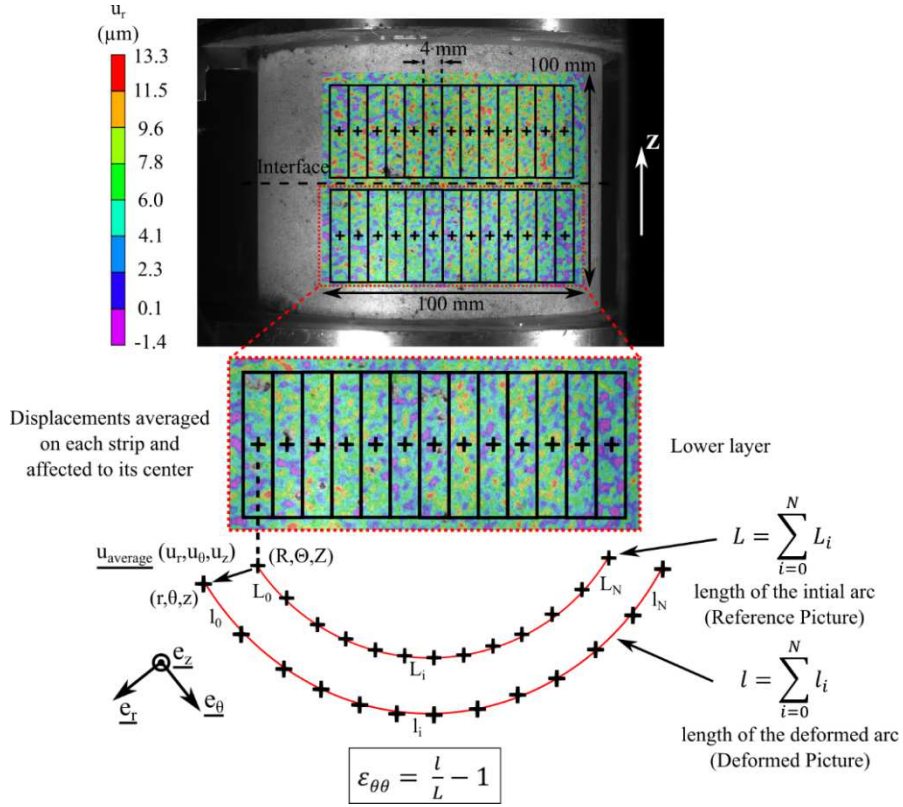


199

200 **Fig. 7.** Vertical displacement  $u_z$  measurements from DIC and illustration of computation of  $\varepsilon_{zz}$  in  
 201 both asphalt layers and of the displacement gap  $\Delta u_z$  at the interface (picture at  $12.5 \mu\text{m}$  in extension)  
 202

203 The strain tensor component  $\varepsilon_{\theta z}$  is obtained using the same method as above, but  
 204 replacing the displacement component  $u_z$  with  $u_\theta$ . The displacement gap  $\Delta u_\theta$  is then  
 205 found. In the analysis method presented in this paper, the interface thickness is consid-  
 206 ered nil, corresponding to a structural point of view. However, it is also possible to use  
 207 DIC to look at the interface from a closer range and to define the thickness of the inter-  
 208 facial transition zone [33]. The latter approach can be used to model interfaces at a  
 209 smaller scale, taking precisely into account aggregate interlocking.

210



211

212 **Fig. 8.** Computation of  $\varepsilon_{\theta\theta}$  in one asphalt layer (picture at 12.5  $\mu\text{m}$  in compression)

213 Assuming that the hollow cylinder remains a hollow cylinder during a test, the strain  
 214 tensor component  $\varepsilon_{\theta\theta}$  is equal to the relative variation of external perimeter of the cyl-  
 215 nder. The computation of  $\varepsilon_{\theta\theta}$  is illustrated in Figure 8. In each layer, about 20 vertical  
 216 strips (4 mm thick and 45 mm high) are drawn on the pictures so that the central points  
 217 of the strips are situated along an arc. Its length in the reference picture can be calcul-  
 218 ated. For each level of deformation, *i.e.* for each picture, the three displacement com-  
 219 ponents ( $u_r$ ,  $u_\theta$ ,  $u_z$ ) of the points in each strip are averaged and affected to the center  
 220 of the strip. The coordinates of the center after transformation are obtained using this av-  
 221 eraged displacement. The centers of the strips after transformation are situated along a  
 222 deformed arc, the length of which is also calculated. The strain tensor component  $\varepsilon_{\theta\theta}$ ,  
 223 equal to the relative variation of arc length, is thus obtained at each state of deformation  
 224 in both asphalt concretes.

225 In the 2T3C HCA, two pairs of cameras are used on opposite sides of the sample.  
 226 The strain tensors components ( $\varepsilon_{\theta\theta}$ ,  $\varepsilon_{zz}$ ,  $\varepsilon_{\theta z}$ ) and the displacement gaps (vertical  $\Delta u_z$   
 227 and rotation  $\Delta u_\theta$ ) are calculated on each side. Then, for each quantity, the two obtained  
 228 values are averaged. The average values are used for the mechanical analysis of the  
 229 sample.

230

### 231 3 Interface mechanical properties

#### 232 3.1 Asphalt complex moduli and complex interface stiffnesses definitions

233 The axial stress  $\sigma_{zz}$  and the shear stress  $\tau_{\theta z}$  in the sample are obtained from load cells  
 234 measurement considering equations (1) and (2). These equations are derived with the  
 235 assumption that stress field is homogeneous in the sample:  
 236

$$\sigma_{zz} = \frac{F}{A} \quad (1)$$

237 where  $F$  is the axial force measured with press load cell and  $A$  the section area of the  
 238 hollow cylinder, and:  
 239

$$\tau_{\theta z} = \frac{3T}{2\pi * (R_{ext}^3 - R_{int}^3)} \quad (2)$$

240 where  $T$  is the torque measured with press load cell,  $R_{ext}$  the external radius and  $R_{int}$  the  
 241 internal radius.

242 For a small number of applied loading cycles and for small loadings amplitudes,  
 243 conditions similar to those existing in a real pavement, asphalt concretes present a linear  
 244 viscoelastic (LVE) behavior [39]. For a sinusoidal loading in stress control mode, the  
 245 LVE material strain response is also a sinusoidal signal with a phase lag.

246 For an axial stress sinusoidal signal  $\sigma_{zz}$  such as equation (3), the strain tensor component  
 247  $\varepsilon_{zz}$  is given in equation (4).  
 248

$$\sigma_{zz}(t) = \sigma_{zz_0} \sin(\omega t) \quad (3)$$

$$\varepsilon_{zz}(t) = \varepsilon_{zz_0} \sin(\omega t - \varphi_E) \quad (4)$$

249 where  $\sigma_{zz_0}$  is the vertical stress amplitude,  $\varepsilon_{zz_0}$  the vertical strain amplitude and  $\varphi_E$  the  
 250 phase angle.

251 The Young's complex modulus  $E_{zz}^*$  is defined in equation (5):

252

$$E_{zz}^* = \frac{\sigma_{zz_0}}{\varepsilon_{zz_0}} e^{i\varphi_E} = |E_{zz}^*| e^{i\varphi_E} \quad (5)$$

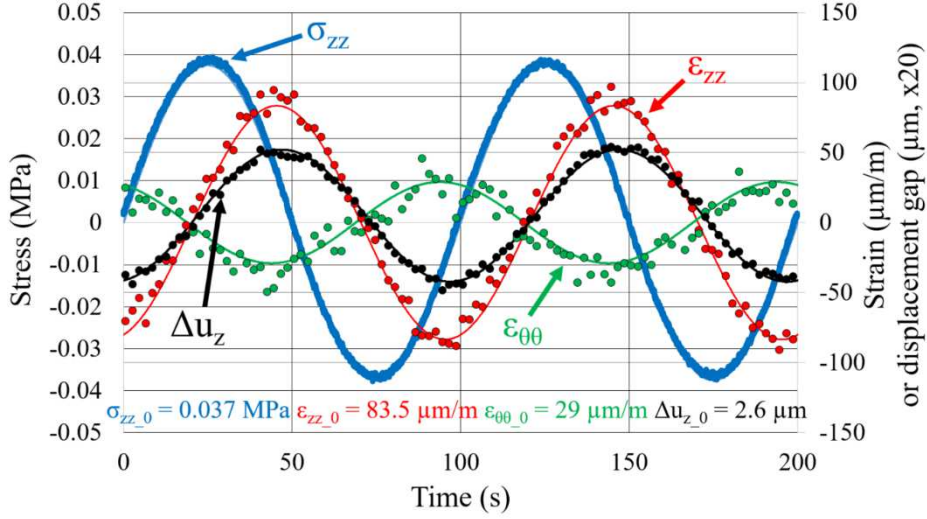
253 When shear stress is applied, for example  $\tau_{\theta z}$  in direction “ $\theta z$ ”, the complex shear  
 254 modulus  $G_{\theta z}^*$  is given in equation (6):

255

$$G_{\theta z}^* = \frac{\tau_{\theta z_0}}{2\varepsilon_{\theta z_0}} e^{i\varphi_G} = |G_{\theta z}^*| e^{i\varphi_G} \quad (6)$$

256 with  $\tau_{\theta z_0}$  the amplitude of shear stress and  $\varepsilon_{\theta z_0}$  the shear strain amplitude.  $\varphi_G$  is the  
 257 phase angle in shear mode.

258



259

260 **Fig. 9.** Example of stress, strain and displacement gap measurements in one layer and at the  
 261 interface for an axial test (with least square approximations in continuous lines)

262 It is observed that when a sinusoidal stress signal is applied to the interface, displace-  
 263 ment gaps are also sinusoidal (as in Figure 9). It is then possible to define a complex  
 264 interface stiffness.

265 The normal complex interface stiffness  $K_{zz}^*$  is defined in equation (7).  
 266

$$K_{zz}^* = \frac{\sigma_{zz,0}}{\Delta u_{z,0}} e^{i\varphi_{Kzz}} = |K_{zz}^*| e^{i\varphi_{Kzz}} \quad (7)$$

267

268 with  $\Delta u_{z,0}$  the amplitude of the vertical displacement gap at the interface.  $\varphi_{Kzz}$  is the  
 269 phase angle for interfaces in tension-compression mode.

270 If torsion is applied, the shear complex interface stiffness  $K_{\theta z}^*$  is given in equation  
 271 (8).  
 272

$$K_{\theta z}^* = \frac{\tau_{\theta z,0}}{\Delta u_{\theta,0}} e^{i\varphi_{K\theta z}} = |K_{\theta z}^*| e^{i\varphi_{K\theta z}} \quad (8)$$

273

274 with  $\Delta u_{\theta,0}$  the amplitude of the horizontal (tangential) displacement gap at the interface.  
 275  $\varphi_{K\theta z}$  is the phase angle for interfaces in shear mode.

276 The complex Poisson's ratio  $\nu_{\theta z}^*$  in each layer can also be found using equation (9):  
 277

$$\nu_{\theta z}^* = \frac{\varepsilon_{\theta\theta,0}}{\varepsilon_{zz,0}} e^{i\varphi_{\nu\theta z}} = |\nu_{\theta z}^*| e^{i\varphi_{\nu\theta z}} \quad (9)$$

278

279 with  $\varepsilon_{\theta\theta,0}$  the amplitude of the relative variation of cylinder perimeter.  $\varphi_{\nu\theta z}$  is the phase  
 angle for Poisson's ratio.

### 280 3.2 Procedure and tested material

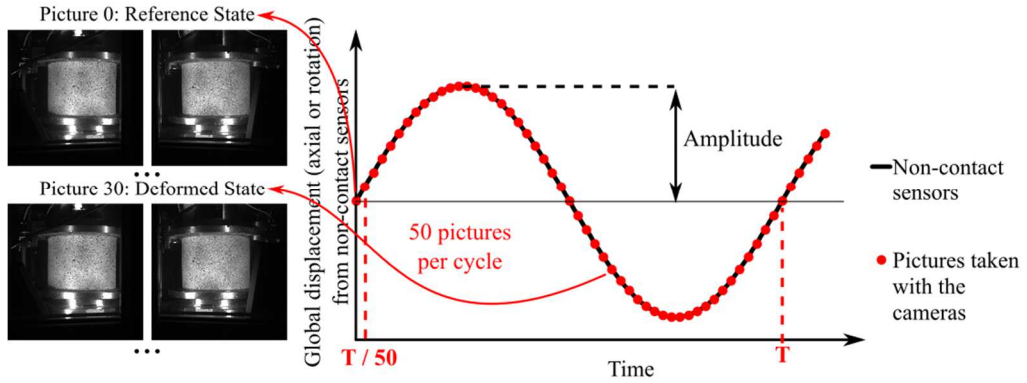
281 One sample with two asphalt concrete layers and a tack coat at the interface has been  
 282 tested. The upper layer was in BBSG3 0/10 [40], representing the wearing course of a  
 283 pavement, and the lower layer was in GB5<sup>®</sup> 0/14, usually used as a base course. The  
 284 two layers had the same thickness. The tack coat is a bituminous emulsion of pure bi-  
 285 tumen with a residual dosage of 350 g/m<sup>2</sup>.

286 In order to characterize the viscoelastic properties of the interface and of the asphalt  
 287 concretes, sinusoidal loading cycles at small strain amplitude were applied to the sam-  
 288 ple. The tests presented in this paper were performed at four different temperatures  
 289 (about 10, 20, 30, and 40 °C). At each temperature, two types of tests were done suc-  
 290 cessively: axial tests and rotation tests (Table 1). During axial tests, vertical displace-  
 291 ment was controlled with the averaged value of the two vertical non-contact sensors  
 292 while torque was maintained nil. During rotation tests, rotation displacement was con-  
 293 trolled with the averaged value of the horizontal non-contact sensors and axial force  
 294 was maintained at a very small compressive value (around 15 kPa). The amplitude val-  
 295 ues for non-contact sensors were calculated in order to get 200  $\mu\text{m/m}$  in global vertical  
 296 strain  $\varepsilon_{zz}$  (corresponding to the case where the sample would be constituted of one ho-  
 297 mogeneous material) for axial tests and 200  $\mu\text{m/m}$  in global shear strain  $\varepsilon_{\theta z}$  for rotation  
 298 tests. For each type of test, four frequencies were tested with five sinusoidal cycles  
 299 applied for each frequency.

300 **Table 1.** Mechanical loading for each temperature

Type of test	Axial loading	Torsion loading	Frequencies (Hz)	Amplitude Non-contact sensors	Cycles per frequency
Axial	Sinusoidal displacement	Zero torque	0.01; 0.03; 0.1; 0.3	$a_x = 25 \mu\text{m}$	5
Rotation	Small compression 15 kPa	Sinusoidal displacement		$rot = 90 \mu\text{m}$	5

301 Each camera took 50 pictures of the sample per cycle (Figure 10) except for cycles  
 302 at 0.3 Hz where 30 pictures were taken at each cycle. The subset size for DIC was  
 303 21 x 21 pixels, which corresponds to 3.1 x 3.1 mm<sup>2</sup> on the material. The capture time  
 304 of a picture was 6 ms.  
 305  
 306



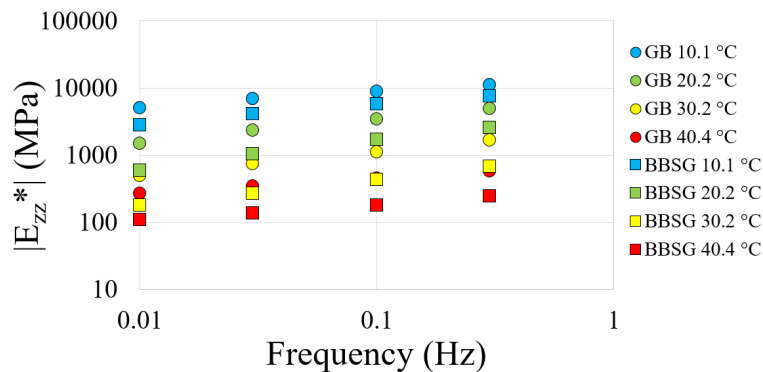
307

308 **Fig. 10.** Global displacement from non-contact sensors and acquisition of pictures on one side  
 309 of the sample during the tests (T is the loading period)

### 310 3.3 Results and discussion

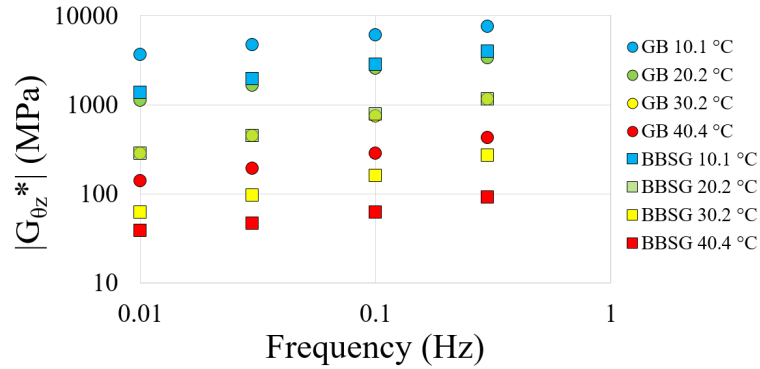
311 All stress and strain signals were fitted with sinusoidal functions using the least  
 312 square method before being analyzed. An indicator was used to quantify and check the  
 313 signal quality. With 3D DIC, the measured vertical strain amplitudes  $\varepsilon_{zz,0}$  for axial tests  
 314 ranged from 200 to 250  $\mu\text{m}/\text{m}$  in the upper layer and from 100 to 150  $\mu\text{m}/\text{m}$  in the  
 315 lower layer, the vertical displacement gap amplitude  $\Delta u_{z,0}$  being between 1 and 3.5  $\mu\text{m}$ .  
 316  $\varepsilon_{\theta\theta}$  amplitude was between 70 and 100  $\mu\text{m}/\text{m}$  in the upper layer and between 25 and 50  
 317  $\mu\text{m}/\text{m}$  in the lower layer. For rotation tests, the shear strain amplitudes  $\varepsilon_{\theta z,0}$  were be-  
 318 tween 250 and 350  $\mu\text{m}/\text{m}$  in the upper layer and between 75 and 100  $\mu\text{m}/\text{m}$  in the lower  
 319 layer, the rotation displacement gap amplitude  $\Delta u_{\theta,0}$  was between 4 and 8  $\mu\text{m}/\text{m}$ . The  
 320 difference in strain values between the two layers is related to the difference in modulus  
 321 between the two asphalt concretes, it depends on the temperature and the frequency.

322 For the asphalt concretes layers, isothermal curves of the Young's complex modulus  
 323 norm  $|E_{zz}^*|$  are shown in the Figure 11 and isothermal curves of the complex shear  
 324 modulus norm  $|G_{\theta z}^*|$  are represented in Figure 12.  
 325



326

327 **Fig. 11.** Isothermal curves of Young's complex modulus norm  $|E_{zz}^*|$  for asphalt concretes in the  
 328 upper layer (BBSG) and in the lower layer (GB)



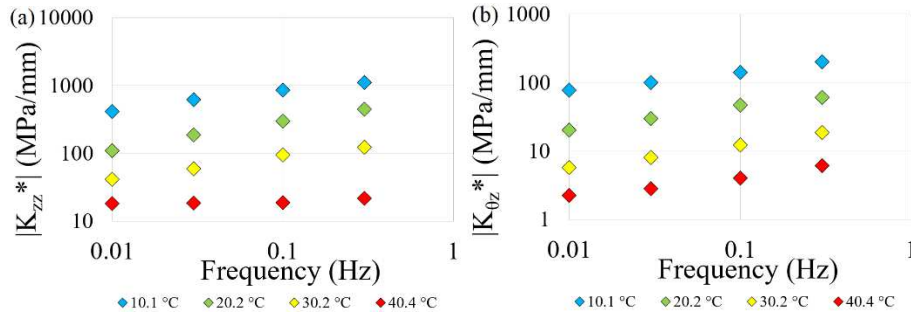
329  
 330

331 **Fig. 12.** Isothermal curves of complex shear modulus  $|G_{\theta z}^*|$  for asphalt concretes in the upper  
 332 layer (BBSG) and in the lower layer (GB)

333 The BBSG 3 asphalt concrete is less rigid than the GB<sup>®</sup> at the same temperature  
 334 and frequency. This can be seen in axial tests (Figure 11) and in rotation tests (Figure  
 335 12) and is consistent with the specifications of these asphalt concretes.

336 Isotherms of normal complex interface stiffness norm  $|K_{zz}^*|$  obtained from axial tests  
 337 and shear complex interface stiffness norm  $|K_{\theta z}^*|$  obtained from the rotation tests are  
 338 presented in Figure 13. Interfaces are more rigid in tension-compression mode than in  
 339 shear mode.

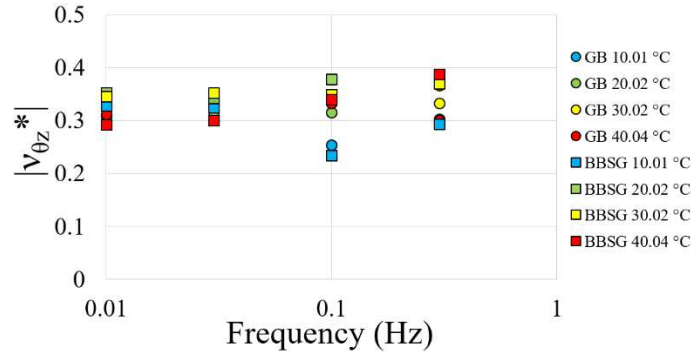
340  
 341



342

343 **Fig. 13.** (a) Isothermal curves of normal complex interface stiffness norm  $|K_{zz}^*|$  for axial tests  
 344 and (b) isothermal curves of shear complex interface stiffness norm  $|K_{\theta z}^*|$  for rotation tests

345 The isotherms of complex Poisson's ratio norm  $|v_{\theta z}^*|$  in the upper (BBSG) layer and  
 346 in the lower (GB) layer are presented in Figure 14 for axial tests. Poisson's ratios values  
 347 are between 0.3 and 0.4 which is a good order of magnitude for asphalt concretes at  
 348 these temperatures and frequencies [41]. No significant differences could be observed  
 349 between the two layers.



350

351  
352

**Fig. 14.** Isothermal curves of complex Poisson's ratio norm  $|v_{\theta z}^*|$  for asphalt concretes in the upper layer (BBSG) and in the lower layer (GB)

## 353 4 Conclusions

354 The 2T3C Hollow Cylinder Apparatus (2T3C HCA) is an innovative prototype with  
 355 unique characteristics to study the interfaces between pavement layers. It can apply  
 356 torsion and/or tension-compression independently to hollow cylinder samples. The  
 357 tests can be cyclic or monotonic with temperature control. The thickness of the wall is  
 358 small regarding the external diameter so the stress distribution can be considered as  
 359 homogeneous in the sample.

360 3D DIC measurements and the developed analysis method enable to obtain the strain  
 361 tensor components ( $\varepsilon_{\theta\theta}$ ,  $\varepsilon_{zz}$ ,  $\varepsilon_{\theta z}$ ) of both asphalt concrete layers and the displacement  
 362 gaps at the interface (vertical  $\Delta u_z$  and rotation  $\Delta u_\theta$ ). The Young's and shear complex  
 363 moduli ( $E_{zz}^*$ ,  $G_{\theta z}^*$ ) and Poisson's ratio ( $v_{\theta z}^*$ ) of the two asphalt mixes and the complex  
 364 interface stiffnesses ( $K_{zz}^*$ ,  $K_{\theta z}^*$ ) are obtained.

365 In this paper, tests at four temperatures (from 10 °C to 40 °C) and four frequencies  
 366 (from 0.01 Hz to 0.3 Hz) in shear mode and in tension-compression mode were per-  
 367 formed on a sample with two asphalt layers and a tack coat at the interface. The follow-  
 368 ing conclusions were drawn from these tests:

369 1) Presented results show the accuracy and efficiency of the 2T3C HCA prototype  
 370 to study interfaces in the small strain domain.

371 2) Displacement gaps with amplitudes as low as 1  $\mu\text{m}$  were observed. Magnitude of  
 372 measured strain amplitude in asphalt layers was of some  $10^{-5}$  m/m.

373 3) The interfaces seem more rigid in tension-compression than in shear.

374 The developed 2T3C HCA device appears as a powerful experimental tool to inves-  
 375 tigate interface properties between bituminous layers.

376

## 377 References

378 1. Uzan, J., Livneh, H. & Eshed, Y. Investigation of adhesion properties between  
 379 asphaltic-concrete layers. in **47**, 495–521 (1978).

- 380 2. Diakhaté, M. Fatigue et comportement des couches d'accrochage dans les struc-  
381 tures de chaussée. (2007).
- 382 3. LCPC & SETRA. *Conception et dimensionnement des structures de chaussée*.  
383 (1994).
- 384 4. AASHTO. *Guide for design of Pavement Structure*. (2002).
- 385 5. Meunier, Y. Le décollement des couches de revêtement de chaussées. (1986).
- 386 6. Blomberg, J. Tack Coat Specifications and Testing. Presented at the North Cen-  
387 tral Asphalt User Producer Group Technical Conference (2014).
- 388 7. Petit, C., Diakhaté, M., Millien, A., Phelipot-Mardelé, A. & Pouteau, B. Pavement  
389 design for curved road sections: fatigue performance of interfaces and longitudinal top-  
390 down cracking in multilayered pavements. *Road Mater. Pavement Des.* **10**, 609–624  
391 (2009).
- 392 8. Leutner, R. Untersuchung des Schichtenverbundes beim bituminösen Oberbau.  
393 **41**, 84–91 (1979).
- 394 9. Tschegg, E. K., Kroyer, G., Tan, D.-M., Stanzl-Tschegg, S. E. & Litzka, J. Invest-  
395 igation of Bonding between Asphalt Layers on Road Construction. *J. Transp. Eng.*  
396 **121**, 309–316 (1995).
- 397 10. Canestrari, F., Ferrotti, G., Partl, M. & Santagata, E. Advanced Testing and  
398 Characterization of Interlayer Shear Resistance. *Transp. Res. Rec. J. Transp. Res.*  
399 *Board* **1929**, 69–78 (2005).
- 400 11. Zofka, A. *et al.* Advanced shear tester for evaluation of asphalt concrete under  
401 constant normal stiffness conditions. *Road Mater. Pavement Des.* **16**, 187–210 (2015).
- 402 12. Zhao, H., Cao, J. & Zheng, Y. Investigation of the interface bonding between  
403 concrete slab and asphalt overlay. *Road Mater. Pavement Des.* **18**, 109–118 (2017).
- 404 13. Brühwiler, E. & Wittmann, F. H. The wedge splitting test, a new method of  
405 performing stable fracture mechanics tests. *Eng. Fract. Mech.* **35**, 117–125 (1990).
- 406 14. Collop, A. C., Sutanto, M. H., Airey, G. D. & Elliott, R. C. Development of an  
407 automatic torque test to measure the shear bond strength between asphalt. *Constr.*  
408 *Build. Mater.* **25**, 623–629 (2011).
- 409 15. Canestrari, F. *et al.* Mechanical Testing of Interlayer Bonding in Asphalt Pave-  
410 ments. in *Advances in Interlaboratory Testing and Evaluation of Bituminous Materials*  
411 (eds Partl, M. N. *et al.*) **9**, 303–360 (Springer Netherlands, 2013).
- 412 16. Raposeiras, A. C., Castro-Fresno, D., Vega-Zamanillo, A. & Rodriguez-Her-  
413 nandez, J. Test methods and influential factors for analysis of bonding between bitumi-  
414 nous pavement layers. *Constr. Build. Mater.* **43**, 372–381 (2013).
- 415 17. Graziani, A., Canestrari, F., Cardone, F. & Ferrotti, G. Time–temperature su-  
416 perposition principle for interlayer shear strength of bituminous pavements. *Road Ma-  
417 ter. Pavement Des.* **18**, 12–25 (2017).
- 418 18. Mohammad, L., Raqib, M. & Huang, B. Influence of asphalt tack coat materi-  
419 als on interface shear strength. *Transp. Res. Rec. J. Transp. Res. Board* 56–65 (2002).
- 420 19. Tozzo, C., D'Andrea, A., Cozzani, D. & Meo, A. Fatigue Investigation of the  
421 Interface Shear Performance in Asphalt Pavement. *Mod. Appl. Sci.* **8**, (2014).
- 422 20. D'Andrea, A. & Tozzo, C. Dynamic tests on bituminous layers interface. *Ma-  
423 ter. Struct.* **49**, 917–928 (2016).
- 424 21. Isailović, I., Wistuba, M., Büchler, S. & Falchetto, A. Interface shear fatigue  
425 performance of asphalt pavement structures in function of normal stress and tempera-  
426 ture. in 1525–1530 (2017). doi:10.1201/9781315100333-218

- 427 22. Raab, C., Partl, M., Fourquet, E. & AbdElHalim, A. Static and cyclic evalua-  
428 tion of interlayer bonding. in *Bearing Capacity of Roads, Railways and Airfields* 1511–  
429 1516 (2017). doi:10.1201/9781315100333-216
- 430 23. Sayao A. & Vaid, Y. P. A critical assessment of stress nonuniformities in hol-  
431 low cylinder test specimens. *Soils Found.* **31**, 60–72 (1991).
- 432 24. Hight, D. W., Gens, A. & Symes, M. J. The development of a new hollow  
433 cylinder apparatus for investigating the effects of principal stress rotation in soils.  
434 *Géotechnique* **33**, 355–383 (1983).
- 435 25. Duttine, A., Di Benedetto, H., Bang, D. P. V. & Ezaoui, A. Anisotropic small  
436 strain elastic properties of sands and mixture of sand-clay measured by dynamic and  
437 static methods. *Soils Found.* **47**, 457–472 (2007).
- 438 26. Sousa, J. B. Dynamic properties of materials for pavement design. (University  
439 of California, Berkeley, 1986).
- 440 27. Brown, S. F., Brodrick, B. V., Tekieli, K. & Collop, A. C. A torsional hollow  
441 cylinder research apparatus for studying the permanent deformation characteristics of  
442 asphalt. *Road Mater. Pavement Des.* **14**, 65–85 (2013).
- 443 28. Rueda, E. J., Caro, S., Caicedo, B. & Monroy, J. A new approach for the ad-  
444 vanced mechanical characterisation of asphalt mixtures using the hollow cylinder meth-  
445 odology. *Measurement* **103**, 333–342 (2017).
- 446 29. NF EN 12697-33+A1 Septembre 2007 Mélange bitumineux - Méthodes d'es-  
447 sai pour mélange hydrocarboné à chaud - Partie 33 : confection d'éprouvettes au com-  
448 pacteur de plaque.
- 449 30. Sutton, M. A., Wolters, W. J., Peters, W. H., Ranson, W. F. & McNeill, S. R.  
450 Determination of displacements using an improved digital correlation method. *Image*  
451 *Vis. Comput.* **1**, 133–139 (1983).
- 452 31. Romeo, E. Two-dimensional digital image correlation for asphalt mixture  
453 characterisation: interest and limitations. *Road Mater. Pavement Des.* **14**, 747–763  
454 (2013).
- 455 32. Buttlar, W. G. *et al.* Digital image correlation techniques to investigate strain  
456 fields and cracking phenomena in asphalt materials. *Mater. Struct.* **47**, 1373–1390  
457 (2014).
- 458 33. Ktari, R., Millien, A., Fouchal, F., Pop, I.-O. & Petit, C. Pavement interface  
459 damage behavior in tension monotonic loading. *Constr. Build. Mater.* **106**, 430–442  
460 (2016).
- 461 34. Golewski, G. L. Estimation of the optimum content of fly ash in concrete com-  
462 posite based on the analysis of fracture toughness tests using various measuring sys-  
463 tems. *Constr. Build. Mater.* **213**, 142–155 (2019).
- 464 35. Golewski, G. L. Measurement of fracture mechanics parameters of concrete  
465 containing fly ash thanks to use of Digital Image Correlation (DIC) method. *Measure-*  
466 *ment.* **135**, 96–105 (2019).
- 467 36. Jin, T., Ha, N. S., Le, V. T., Goo, N. S. & Jeon, H. C. Thermal buckling meas-  
468 urement of a laminated composite plate under a uniform temperature distribution using  
469 the digital image correlation method. *Compos. Struct.* **123**, 420–429 (2015).
- 470 37. Chemisky, Y., Meraghni, F., Bourgeois, N., Cornell, S., Echchorfi, R. & Pa-  
471 toor, E. Analysis of the deformation paths and thermomechanical parameter identifica-  
472 tion of a shape memory alloy using digital image correlation over heterogeneous tests.  
473 *Int. J. Mech. Sci.* **96-97**, 13–24 (2015).

- 474       38. Sutton, M. A., McNeill, S. R., Helm, J. D. & Chao, Y. J. Advances in two-  
475 dimensional and three-dimensional computer vision. in *Photomechanics* 323–372  
476 (2000).
- 477       39. Gayte, P., Di Benedetto, H., Sauzéat, C. & Nguyen, Q. T. Influence of transient  
478 effects for analysis of complex modulus tests on bituminous mixtures. *Road Mater.*  
479 *Pavement Des.* **17**, 271–289 (2016).
- 480       40. NF EN 13108-1 Septembre 2007 Mélange bitumineux - Spécification des ma-  
481 tériaux - Partie 1 : Enrobés bitumineux.
- 482       41. Perraton, D. *et al.* 3Dim experimental investigation of linear viscoelastic prop-  
483 erties of bituminous mixtures. *Mater. Struct.* **49**, 4813–4829 (2016).  
484